

p -MULTILEVEL MONTE CARLO FOR ACOUSTIC SCATTERING FROM LARGE DEVIATION ROUGH RANDOM SURFACES

JÜRGEN DÖLZ, WEI HUANG, AND MICHAEL MULTERER

ABSTRACT. We study time harmonic acoustic scattering on large deviation rough random scatterers. Therein, the roughness of the scatterers is caused by a low Sobolev regularity in the covariance function of their deformation field. The motivation for this study arises from physical phenomena where small-scale material defects can potentially introduce non-smooth deviations from a reference domain. The primary challenge in this scenario is that the scattered wave is also random, which makes computational predictions unreliable. Therefore, it is essential to quantify these uncertainties to ensure robust and well-informed design processes. While existing methods for uncertainty quantification typically rely on domain mapping or perturbation approaches, it turns out that large and rough random deviations are not satisfactorily covered. To close this gap, and although counter intuitive at first, we show that the p -multilevel Monte Carlo method can provide an efficient tool for uncertainty quantification in this setting. To this end, we discuss the stable implementation of higher-order polynomial approximation of the deformation field by means of barycentric interpolation and provide a cost-to-accuracy analysis. Our considerations are complemented by numerical experiments in three dimensions on a complex scattering geometry.

1. INTRODUCTION

1.1. Motivation. We consider time harmonic, sound-soft acoustic scattering where the scatterer is a bounded obstacle. We assume that the scatterer $D(\omega) \subset \mathbb{R}^3$ is given as a large and rough random deviation of Karhunen-Loève-type from a reference domain D_0 with Lipschitz boundary. Here, we consider a deviation as rough if the covariance function of the deformation field has low Sobolev regularity. This setting is motivated by the fact that in reality defects in the scatterer's surface often happen on a relatively small scale and may even induce non-smooth artifacts in a previously smooth surface. Considering a plane incident wave $u_{\text{inc}}(\mathbf{x}) = e^{-i\kappa\langle \mathbf{d}, \mathbf{x} \rangle}$ with known wavenumber κ and direction \mathbf{d} , where $\|\mathbf{d}\|_2 = 1$, the total wave $u = u_{\text{inc}} + u_s(\omega)$ around the scatterer is obtained by solving the exterior boundary value problem

$$(1) \quad \begin{aligned} \Delta u + \kappa^2 u &= 0 && \text{in } \mathbb{R}^3 \setminus \overline{D(\omega)}, \\ u &= 0 && \text{on } S(\omega) = \partial D(\omega), \\ \sqrt{r} \left(\frac{\partial u_s(\omega)}{\partial r} - i\kappa u_s(\omega) \right) &\rightarrow 0 && \text{as } r = \|\mathbf{x}\|_2 \rightarrow \infty, \end{aligned}$$

to obtain the scattered wave $u_s(\omega)$. The sound-hard case can be treated in complete analogy, see for example [18].

The main difficulty in the described situation is that the scattered wave $u_s(\omega)$ is also random. To ensure robust and well-informed design processes in engineering and the applied sciences, it is of utmost importance to quantify these uncertainties. Due to the complexity of most underlying partial differential equations and the arising uncertainty, this needs to be achieved by means of numerical algorithms.

1.2. State-of-the-art. Pioneering works on the acoustic scattering problem by deterministic scatterers with roughness on a small scale have been of interest for a long time with pioneering works going back to [33, 34, 38], see also [13] and the references therein for a recent review. However, to the best of our knowledge, there are very scarce investigations into the acoustic scattering problem by rough random scatterers, especially in case of complex three-dimensional obstacles.

Within the mathematical community for uncertainty quantification, there have been significant contributions to develop algorithms quantifying this uncertainty in the solution to partial differential equations on random domains, mainly by computing statistical moments. These contributions can roughly be categorized into domain mapping approaches and perturbation approaches. Domain mapping approaches [1, 10, 16, 19, 27, 30, 32, 40] transfer the shape uncertainty into randomly varying coefficients on a fixed reference domain. This allows to deal with large domain deformations and the computation of statistical moments by evaluating the corresponding high-dimensional integrals, typically employing sampling based quadrature methods. Unfortunately, this requires the realization of a random domain and solving a partial differential equation thereon for each sample, which can be quite expensive. To reduce the number of required samples, quasi-Monte Carlo (QMC) methods [8] and sparse grids [6] exploit parametric smoothness and may be combined with multilevel sampling techniques [22, 26]. Perturbation approaches compute the statistical moments by approximating them with truncated Taylor expansions in the Fréchet sense [5, 14, 15, 28]. The additional correction terms can often be computed without the need for high-dimensional quadrature methods. Although perturbation approaches have the potential to deal with rough domain deformations, the obtained results are usually only reliable when the domain deformations are small. A combination of the two approaches was presented in [11, 35], but relies on an a-priorily available splitting of the domain deformations into small and large amplitudes of the deformations. Summarizing, state-of-the-art methods rely on different kinds of smoothness and can either work with large and rather global or with small and rough randomness in the shape of the domain.

1.3. Challenges when dealing with rough random shapes. The situation which is left out in the scope of currently available methods is the case when the domain deformations are rough and possibly large. This setting implies a number of challenges:

- (1) QMC and sparse grids do not work: The low Sobolev regularity leads to a slow decay of the eigenvalues of the associated covariance operator, leading to a true high-dimensionality of the parameter

space. Indeed, the decay in the parametric dimension is such that QMC and sparse grid methods are no longer efficiently applicable.

- (2) Perturbation approaches are not suitable: The main assumption of perturbation approaches, that the amplitude of the perturbations is suitably small, is not necessarily fulfilled for rough domain deformations. The prime example are domain deformations described by the Matérn-1/2 kernel, which is not differentiable on the diagonal but can model arbitrarily large domain deformations.
- (3) Resolving rough surfaces is expensive: It is well known that the numerical approximation of rough surface domains requires lower or lowest order polynomials on relatively refined meshes close to the roughness. Similar considerations hold for functions defined on these domains, and in particular for the solutions of partial differential equations thereon. This leads to a large number of degrees of freedom and thus to large computational cost per sample.

In view of the above literature review, the only available option in this case is to use a Monte Carlo sampling strategy on a set of highly refined samples. However, this approach is computationally not feasible.

1.4. Contribution. The purpose of this article is to illustrate on the example of acoustic scattering that the p -multilevel Monte Carlo method (p -MLMC), see [4], has the potential to alleviate the aforementioned challenges. By p -MLMC we refer to a construction of the required multilevel hierarchy by increasing the polynomial degree of the ansatz spaces, rather than various mesh hierarchies. To this end, we

- (1) discuss the stable and efficient shape discretization by higher-order polynomials and barycentric interpolation,
- (2) perform a required sample to accuracy analysis for the p -MLMC,
- (3) provide numerical numerical examples in three-dimensions on a complex geometry.

The use of a higher-order polynomial approximation method may seem unintuitive at first, but can be motivated quite naturally. To this end, we curiously observe that, on smooth surfaces, the eigenfunctions of covariance integral operators are always smooth, even if the covariance function itself is not. Thus, when the Karhunen-Lève expansion is truncated for numerical computations, the resulting deformation field, the deformed domain, and the solution to the scattering problem will always be smooth. We can thus expect exponential convergence in the polynomial degree if higher-order schemes are used.

1.5. Outline. The remainder of this article is structured as follows. Section 2 introduces the modeling of rough random domains using Matérn kernels with low smoothness index and their representation by the Karhunen-Loève expansion. Section 3 explores the conversion of a complex geometry, i.e., Michelangelo's David, from a triangular mesh to a NURBS representation and discusses its further high-order polynomial re-interpolation. Moreover, the discretization of random deformation fields by barycentric interpolation is introduced. In Section 4, we revisit the boundary integral formulation of the problem and the computation of quantities of interest (QoI), as described

in [16]. Section 5 introduces the p -MLMC method and determines the optimal scaling factors for increasing polynomial degrees. Section 6 presents extensive numerical studies conducted on a torus and the David geometry. Concluding remarks are stated in Section 7.

2. ROUGH RANDOM DOMAIN MODEL

2.1. Modelling of random surfaces. Let $(\Omega, \mathcal{F}, \mathbb{P})$ denote a complete probability space. For the modelling of random domains, we assume the existence of a Lipschitz continuous reference surface S_0 bounding the reference domain $D_0 \subset \mathbb{R}^D$ and a random deformation field

$$\chi: \Omega \times S_0 \rightarrow \mathbb{R}^3$$

such that there exists a constant $C_{\text{uni}} > 0$ with

$$\|\chi(\omega)\|_{C^1(S_0; \mathbb{R}^3)}, \|\chi^{-1}(\omega)\|_{C^1(S(\omega); \mathbb{R}^3)} \leq C_{\text{uni}}$$

and

$$S(\omega) = \chi(\omega, S_0) \quad \text{for } \mathbb{P}\text{-a.e. } \omega \in \Omega.$$

We make the practical assumption that the random deformation field χ is known by its first- and second- order spatial statistics, i.e., its expected deformation field

$$\mathbb{E}[\chi]: S_0 \rightarrow \mathbb{R}^3$$

and its matrix-valued covariance function

$$\text{Cov}[\chi]: S_0 \times S_0 \rightarrow \mathbb{R}^{3 \times 3}.$$

Without loss of generality, we assume that $\mathbb{E}[\chi](\mathbf{x}) = \mathbf{x}$. Otherwise, the reference domain has to be appropriately mapped, see [27]. The components of the covariance function is modeled by Matérn covariance functions of some order $\nu > 0$. They are given by

$$k_\nu(r) := \frac{2^{1-\nu}}{\Gamma(\nu)} \left(\frac{\sqrt{2\nu}r}{l} \right)^\nu K_\nu \left(\frac{\sqrt{2\nu}r}{l} \right),$$

The eigenvalues of these kernels asymptotically decay like

$$(2) \quad \lambda_j \leq C j^{-(1+\frac{2\nu}{d})},$$

where d is the spatial dimension, see e.g. [23]. In particular, the eigenvalues of the Gaussian kernel ($\nu = \infty$) decay exponentially. Later on, we shall employ the smooth Gaussian kernels to model smooth deformations, while rougher kernels (with smaller ν , and thus a slower eigenvalue decaying rate) are used to represent rough deformations.

We remark that in our particular case of a two-dimensional manifold, when $\nu \leq 5$, neither the Halton sequence, see [7, 39], nor the anisotropic sparse grid quadrature, see [24], are dimension robust due to the insufficient decay of the deformation field's Karhunen-Loève expansion. Therefore, we exclusively consider the Monte Carlo method in this article.

2.2. Representation of random deformation fields. In this section, we recall the ideas presented in [16, 31]. As has been argued there, it is sufficient to compute the Karhunen-Loève expansion of the random deformation field exclusively with respect to the random surface and no volume discretization is required at all. Hence, given the expected deformation field $\mathbb{E}[\chi]$ and its matrix-valued covariance function $\text{Cov}[\chi]$, we can compute the surface Karhunen-Loève expansion

$$\chi(\omega, \mathbf{x}) = \mathbb{E}[\chi](\mathbf{x}) + \sum_{k=1}^{\infty} \sqrt{\lambda_k} \chi_k(\mathbf{x}) Y_k(\omega), \quad \mathbf{x} \in S_0.$$

Herein, the tuples $\{(\lambda_k, \chi_k)\}_k$ are the eigenpairs of the covariance operator

$$\begin{aligned} \mathcal{C}: [L^2(S_0)]^3 &\rightarrow [L^2(S_0)]^3, \\ (\mathcal{C}\mathbf{v})(\mathbf{x}) &:= \int_{S_0} \text{Cov}[\chi](\mathbf{x}, \mathbf{x}') \mathbf{v}(\mathbf{x}') d\sigma_{\mathbf{x}'} \end{aligned}$$

and, for $\lambda_k \neq 0$, the centred and uncorrelated random variables $\{Y_k\}_k$ are given according to

$$Y_k(\omega) := \frac{1}{\sqrt{\lambda_k}} \int_{S_0} (\chi(\omega, \mathbf{x}) - \mathbb{E}[\chi](\mathbf{x}))^\top \chi_k(\mathbf{x}) d\sigma_{\mathbf{x}}.$$

In practice, however, the random variables $\{Y_k\}_k$ are not known explicitly and need to be estimated. We make the common model assumption that the random variables $\{Y_k\}_k$ are independent and uniformly distributed with $Y_k \sim \mathcal{U}(-1, 1)$ for all k . For numerical computations, the Karhunen-Loève expansion has to be truncated after $m \in \mathbb{N}$ terms, where m has to be chosen to meet an acceptable accuracy. Then, by identifying each random variable Y_k by its image $y_k \in [-1, 1]$, we arrive at the parametric deformation field

$$(3) \quad \chi(\mathbf{y}, \mathbf{x}) = \mathbb{E}[\chi](\mathbf{x}) + \sum_{k=1}^m \sqrt{\lambda_k} \chi_k(\mathbf{x}) y_k, \quad \mathbf{y} \in \Gamma := [-1, 1]^m.$$

The parametric deformation field gives rise to the parametric surfaces

$$(4) \quad S(\mathbf{y}) = \{\chi(\mathbf{y}, \mathbf{x}) : \mathbf{x} \in S_0\}.$$

3. DISCRETIZATION OF ROUGH RANDOM DOMAINS

3.1. Surface representation of complex geometries. We assume the usual isogeometric setting for the surface S_0 of the reference domain D_0 . The surface S_0 can be decomposed into several smooth *patches*

$$S_0 = \bigcup_{i=1}^M S_0^{(i)}.$$

The intersection $S_0^{(i)} \cap S_0^{(i')}$ consists at most of a common vertex or a common edge for $i \neq i'$. In particular, each patch $S_0^{(i)}$ is the image of an invertible NURBS mapping

$$(5) \quad \mathbf{s}_i: \square \rightarrow S_0^{(i)} \quad \text{with} \quad S_0^{(i)} = \mathbf{s}_i(\square) \quad \text{for } i = 1, 2, \dots, M,$$

where \mathbf{s}_i is of the form

$$\mathbf{s}_i(x, y) := \sum_{0=i_1}^{k_1} \sum_{0=i_2}^{k_2} \frac{\mathbf{c}_{i_1, i_2} b_{i_1}^{p_1}(x) b_{i_2}^{p_2}(y) w_{i_1, i_2}}{\sum_{j_1=0}^{k_1-1} \sum_{j_2=0}^{k_2-1} b_{j_1}^{p_1}(x) b_{j_2}^{p_2}(y) w_{j_1, j_2}}$$

for control points $\mathbf{c}_{i_1, i_2} \in \mathbb{R}^3$ and weights $w_{i_1, i_2} > 0$, where $\{b_{i_1}^{p_1}\}_{0 \leq i_1 < k_1}$ and $\{b_{i_2}^{p_2}\}_{0 \leq i_2 < k_2}$ are the B-spline basis. We shall further follow the common convention that parametrizations with a common edge coincide except for orientation.

We remark that such a surface representation is often not directly available for more complex geometries. Instead, what we usually have are triangular meshes. The partitioning of surface meshes into conforming quadrilateral patches can be solved by a workflow, which is based on determining a suitable set of nodes called *singularities* and connecting these by a set of arcs called *separatrices*, such that the resulting partition consists of multiple valid conforming quadrilateral patches, see [9, 20] and the references therein. As a challenging geometry, we consider the head of Michelangelo's David are used in this paper. The initial geometry is a surface mesh from a 3D scan (the scan is provided by the Statens Museum for Kunst under the Creative Commons CC0 license). Starting from a triangular mesh, we compute the critical points of the eigenfunctions of the Laplace-Beltrami operator. The critical points correspond to the geometric singularities. Next, we transform the triangular mesh into quadrangulations via the discrete Morse-Smale algorithm, which is available as `Python` library `Topology ToolKit`, see [3, 37]. Finally, we obtain conforming quad patches by tracing separatrices starting from the critical points, followed by a subsequent approximation of each patch by NURBS surfaces, see Figure 1. Specifically, we use the 340-th largest eigenfunction of the Laplace-Beltrami operator on David's surface, which results in 187 patches in total.

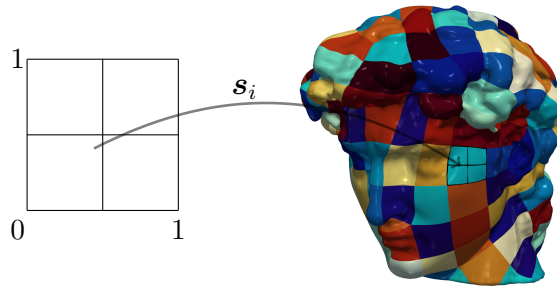


FIGURE 1. NURBS surface representation of Michelangelo's David. The spatial refinement level is $\ell = 1$ on \square .

Regarding the boundary element solver, we define the ansatz space on S_0 by patchwise lifting the standard B-spline basis space on the unit square. The same concept can be applied on the rough random surface $S(\omega)$, see [31] for the details. The spatial level of uniform refinement on the unit square is denoted by ℓ , and the degree of the B-spline used is indicated by p .

Throughout the article, we fix $\ell = 1$ and refine p for increasing the accuracy of solutions.

3.2. Barycentric interpolation. We focus on the situation that the NURBS patches under consideration are smooth, i.e., polynomial. Therefore, we may employ a polynomial model to represent the random deformation field. We start by re-interpolating the patches $\mathbf{s}_i: \square \rightarrow S_0$. To this end, given a polynomial degree q , we introduce the Chebyshev points of the second kind

$$(6) \quad \xi_k := \frac{1}{2} \left(1 - \cos \frac{k\pi}{q} \right), \quad k = 0, \dots, q.$$

We denote the corresponding Lagrange polynomials by

$$L_k(s) := \prod_{j \neq k} \frac{s - \xi_j}{\xi_k - \xi_j}.$$

The corresponding interpolation points on the unit square are then given by a tensor product construction according to

$$\boldsymbol{\xi}_{k,k'} := \begin{bmatrix} \xi_k \\ \xi_{k'} \end{bmatrix} \in \square.$$

The mapped points

$$\mathbf{p}_{i,k,k'} := \mathbf{s}_i(\boldsymbol{\xi}_{k,k'})$$

serve as landmark points for the representation of the random surface. The set of all landmark points is denoted by

$$(7) \quad \boldsymbol{\Theta} := \{\mathbf{p}_{i,k,k'} : 1 \leq i \leq M, 0 \leq k, k' \leq q\}.$$

The deformation field is now represented according to

$$\boldsymbol{\chi}(\omega, \mathbf{s}_i(s, t)) \approx \sum_{k=0}^q \sum_{k'=0}^q \boldsymbol{\chi}(\omega, \mathbf{p}_{i,k,k'}) L_k(s) L_{k'}(t).$$

To obtain a stable polynomial interpolation also for a large number of landmark points, we employ the barycentric interpolation formula from [2]. Factoring out the node polynomial and regarding that the Lagrange polynomials form a partition of unity yields the one-dimensional polynomial interpolant of the function $f: [0, 1] \rightarrow \mathbb{R}$ by means of the representation

$$(8) \quad p(s) = \rho(s) \sum_{k=0}^q \frac{w_k}{s - \xi_k} f(\xi_k), \quad \rho(s) := \left(\sum_{k=0}^q \frac{w_k}{s - \xi_k} \right)^{-1}.$$

Herein, the weights are given by

$$w_k := \prod_{j \neq k} \frac{1}{\xi_k - \xi_j}.$$

For the Chebyshev points of the second kind, the weights can be precomputed by the formula, cp. [36],

$$w_k = (-1)^k \delta_k, \quad \text{where } \delta_k := \begin{cases} 0.5, & \text{if } k = 0, q, \\ 1, & \text{else.} \end{cases}$$

Obviously, the weights are invariant under affine transforms, as any such transforms cancels out due to the barycentric formula. Moreover, in the concrete case, the weights are also invariant under the reversal of the order

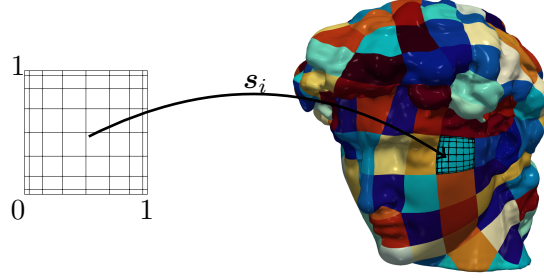


FIGURE 2. Tensor product of the Chebyshev points of the second kind and surface re-interpolation by polynomials of degree $q = 8$.

of the interpolation nodes, as we have tacitly done in the definition (6). Now, tensorizing the univariate interpolant (8) yields the final representation

$$(9) \quad \chi(\omega, \mathbf{s}_i(s, t)) \approx \rho(s)\rho(t) \sum_{k,k'=0}^q \frac{w_k}{s - \xi_k} \frac{w'_k}{s - \xi_{k'}} \chi(\omega, \mathbf{p}_{i,k,k'}).$$

Here, the polynomial degree q is always chosen such that the overall consistency error is met. An example of the re-interpolation of David is shown in Figure 2.

3.3. Discretization of random deformation fields. The landmark points for the re-interpolation are also used to discretize the covariance operator. To evaluate the Karhunen-Loève expansion at the landmark points in Θ from (7), we have to solve the eigenvalue problem for the covariance matrix

$$\mathbf{C} := [\text{Cov}[\chi](\mathbf{x}, \mathbf{x}')]_{\mathbf{x}, \mathbf{x}' \in \Theta} \in \mathbb{R}^{3n \times 3n},$$

where we set $n := |\Theta|$. Because solving the eigenvalue problem is of cost $\mathcal{O}(n^3)$, we first use a low-rank approach via the pivoted Cholesky decomposition, see [25]. Having $\mathbf{C} \approx \mathbf{L}\mathbf{L}^\top$, $\text{rank } \mathbf{L} = m \ll 3n$, we solve

$$\mathbf{L}\mathbf{L}^\top \mathbf{v} = \lambda \mathbf{v} \quad \text{via} \quad \mathbf{L}^\top \mathbf{L} = \tilde{\mathbf{V}} \mathbf{\Lambda} \tilde{\mathbf{V}}^\top.$$

Given that $(\lambda, \tilde{\mathbf{v}}_i)$ is an eigenpair of the latter, $(\lambda_k, \mathbf{L}\tilde{\mathbf{v}}_k)$ is an eigenpair of the former. Finally, we obtain the representation of the random deformation at the landmarks defined by

$$(10) \quad \chi(\omega, \Theta) = \Theta + \alpha \cdot \text{reshape}(\mathbf{L}\tilde{\mathbf{V}}\mathbf{y}, 3, n).$$

Herein, α is the magnitude of the random deformation, which steers the impact of the random deformation, and \mathbf{y} satisfies the uniform distribution in $[-1, 1]^m$.

In summary, having a NURBS representation of the scatterer's surface, we first re-interpolate each patch at once with a tensor product of Lagrange polynomials of degree q . Then, we compute a low-rank approximation of the rough random deformation field evaluated at the landmark points via the pivoted Cholesky decomposition. Finally, the geometry deformations are obtained by updating the landmark points using (10) and re-interpolation via (9).

4. SCATTERING AT RANDOM OBSTACLES

4.1. Boundary integral equations. In this section, we recall the computation of scattered waves (1) for each realization of the rough random scatterer using boundary integral equations. Throughout the paper, the scattered wave $u_s(\omega)$, the total wave $u(\omega)$, the scatterer $D(\omega)$, and the corresponding surface $S(\omega)$ are all dependent on the stochastic term ω . For simplicity of notation, we omit the term ω in this paragraph.

We introduce the acoustic single layer operator

$$\mathcal{V}: H^{-1/2}(S) \rightarrow H^{1/2}(S), \quad (\mathcal{V}\rho)(\mathbf{x}) := \int_S \Phi(\mathbf{x}, \mathbf{z}) \rho(\mathbf{z}) d\sigma_{\mathbf{z}},$$

and the acoustic double layer operator

$$\mathcal{K}: L^2(S) \rightarrow L^2(S), \quad (\mathcal{K}\rho)(\mathbf{x}) := \int_S \frac{\partial \Phi(\mathbf{x}, \mathbf{z})}{\partial \mathbf{n}_z} \rho(\mathbf{z}) d\sigma_{\mathbf{z}}.$$

Herein, \mathbf{n}_z denotes the outward pointing normal vector at the surface point $\mathbf{z} \in S$, while $\Phi(\cdot, \cdot)$ denotes the fundamental solution for the Helmholtz equation. In our case, the fundamental function is given by

$$\Phi(\mathbf{x}, \mathbf{z}) = \frac{e^{-i\kappa \|\mathbf{x} - \mathbf{z}\|_2}}{4\pi \|\mathbf{x} - \mathbf{z}\|_2}.$$

Considering an incident plane wave $u_{\text{inc}}(\mathbf{x}) = e^{-i\kappa \langle \mathbf{d}, \mathbf{x} \rangle}$, $\|\mathbf{d}\|_2 = 1$, the Neumann data of the total wave $u = u_{\text{inc}} + u_s$ at the surface S can be determined by the boundary integral equation

$$\left(\frac{1}{2} + \mathcal{K}^* - i\eta \mathcal{V} \right) \frac{\partial u}{\partial \mathbf{n}} = \frac{\partial u_{\text{inc}}}{\partial \mathbf{n}} - i\eta u_{\text{inc}} \quad \text{on } S,$$

with $\eta = \kappa/2$, cp. [12].

From the Cauchy data of u at S , we can determine the scattered wave u_s at any exterior point outside the obstacle by applying the potential evaluation

$$(11) \quad u_s(\mathbf{x}) = \int_S \Phi(\mathbf{x}, \mathbf{z}) \frac{\partial u}{\partial \mathbf{n}_z}(\mathbf{z}) d\sigma_{\mathbf{z}}, \quad \mathbf{x} \in \mathbb{R}^3 \setminus \bar{D}.$$

In Figure 3, we visualise one example of a scattered wave by Michelangelo's David.

4.2. Scattered wave representation at an artificial interface. As proposed in [16], we introduce an artificial interface $T \subset \mathbb{R}^3$, being sufficiently large to guarantee that T encloses all realizations of the domain D . Applying (11) yields the Dirichlet data of the scattered wave at the artificial interface, i.e., $u_s|_T$. With regard to the Neumann data $(\partial u_s / \partial \mathbf{n})|_T$, we may take the normal derivative of (11) at T , which yields

$$\frac{\partial u_s}{\partial \mathbf{n}_x}(\mathbf{x}) = \int_S \frac{\partial \Phi(\mathbf{x}, \mathbf{z})}{\partial \mathbf{n}_x} \frac{\partial u}{\partial \mathbf{n}_z}(\mathbf{z}) d\sigma_{\mathbf{z}}, \quad \mathbf{x} \in T.$$

Having the Cauchy data on T , the representation formula for T is given by

$$(12) \quad u_s(\mathbf{x}) = \int_T \left\{ \frac{\partial \Phi(\mathbf{x}, \mathbf{z})}{\partial \mathbf{n}_z} u_s(\mathbf{z}) - \Phi(\mathbf{x}, \mathbf{z}) \frac{\partial u_s}{\partial \mathbf{n}_z}(\mathbf{z}) \right\} d\sigma_{\mathbf{z}},$$

see [12]. Then, we may evaluate scattered wave outside T applying (12) for T instead of (11) for S .

The significant advantage of (12) over (11) is that the artificial interface and the function space at T are fixed in contrast to the shape of the random obstacle and non-nested hierarchical B-spline function spaces of increasing polynomial degrees, respectively.

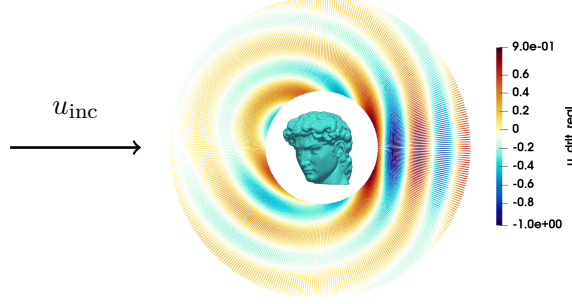


FIGURE 3. It shows the real part of the scattering waves by Davide in the case of an incident plane wave with wavenumber $\kappa = 5$ and direction $\mathbf{d} = [1, 0, 0]^\top$.

4.3. Quantities of interest. It is sufficient to compute the first and second moments of the Cauchy data at the artificial interface T for knowing the statistics at the points outside T . We recall the formulas here. For any $\mathbf{x} \in \mathbb{R}^3$ lying outside the interface T , it holds

$$\mathbb{E}[u_s](\mathbf{x}) = \int_T \left\{ \frac{\partial \Phi(\mathbf{x}, \mathbf{z})}{\partial \mathbf{n}_z} \mathbb{E}[u_s](\mathbf{z}) - \Phi(\mathbf{x}, \mathbf{z}) \mathbb{E} \left[\frac{\partial u_s}{\partial \mathbf{n}_z} \right](\mathbf{z}) \right\} d\sigma_z.$$

With respect to the covariance, we find for two points $\mathbf{x}, \mathbf{x}' \in \mathbb{R}^3$ lying outside of the interface T the deterministic expression

$$\begin{aligned} \text{Cor}[u_s](\mathbf{x}, \mathbf{x}') = \int_T \int_T \left\{ \Phi(\mathbf{x}, \mathbf{z}) \overline{\Phi(\mathbf{x}', \mathbf{z}')} \text{Cor} \left[\frac{\partial u_s}{\partial \mathbf{n}} \right](\mathbf{z}, \mathbf{z}') \right. \\ - \Phi(\mathbf{x}, \mathbf{z}) \frac{\partial \overline{\Phi(\mathbf{x}', \mathbf{z}')}}{\partial \mathbf{n}_{z'}} \text{Cor} \left[\frac{\partial u_s}{\partial \mathbf{n}}, u_s \right](\mathbf{z}, \mathbf{z}') \\ - \frac{\partial \Phi(\mathbf{x}, \mathbf{z})}{\partial \mathbf{n}_z} \overline{\Phi(\mathbf{x}', \mathbf{z}')} \text{Cor} \left[u_s, \frac{\partial u_s}{\partial \mathbf{n}} \right](\mathbf{z}, \mathbf{z}') \\ \left. + \frac{\partial \Phi(\mathbf{x}, \mathbf{z})}{\partial \mathbf{n}_z} \frac{\partial \overline{\Phi(\mathbf{x}', \mathbf{z}')}}{\partial \mathbf{n}_{z'}} \text{Cor}[u_s](\mathbf{z}, \mathbf{z}') \right\} d\sigma_{z'} d\sigma_z. \end{aligned}$$

5. p -MULTILEVEL MONTE CARLO METHOD

To compute QoIs, we rely on the Monte Carlo method, whose expected error is proportional to $N^{-1/2}$, where N is the number of samples, given that the integrand has bounded variance. To speed up the Monte Carlo method, we employ the p -MLMC method. This approach constructs a sequence of control variates for variance reduction of the integrand. This variance reduction is achieved by the decreasing spatial approximation error with

respect to the polynomial degree p . This error decreases even exponentially given that all involved quantities are smooth.

The sequence of control variates in the multilevel Monte Carlo method is based on a telescoping sum, see e.g. [21, 22, 29]. We adapt their approach to the multilevel method for p -refinement, which yields the and approximation for each of the two QoIs. In both cases we refer to \mathcal{Q}_{P-p} to the Monte Carlo quadrature operator associated to the polynomial degree p , where P is the maximum degree. For the expectation of the quantity $\rho^{(P)}$, we employ the estimator

$$\mathbb{E}[\rho](z) \approx \sum_{p=0}^P \mathcal{Q}_{P-p}(\rho^{(p)}(\cdot, z) - \rho^{(p-1)}(\cdot, z)),$$

while its correlation is computed by

$$\text{Cor}[\rho \otimes \mu](z, z') \approx \sum_{p=0}^P \mathcal{Q}_{P-p}((\rho \otimes \mu)^{(p)}(\cdot, z, z') - (\rho \otimes \mu)^{(p-1)}(\cdot, z, z')).$$

The sequence of $\{\rho^{(p)}\}$ approximates ρ with not only increasing accuracy but also increasing cost. Besides, we assume the variance of the difference $\rho^{(p)} - \rho^{(p-1)}$ between two consecutive levels decreases with respect to p . We recall that in p -refinement, the levels indicate the degrees of B-spline basis. By computing relatively few samples at the high levels but lots of samples at the coarse levels, we substantially save in terms of the total computations, see [22]. In particular, if we use N_p samples for \mathcal{Q}_{P-p} , we can rewrite the formula for the expectation according to

$$\mathbb{E}[\rho](z) \approx N_0^{-1} \sum_{n=1}^{N_0} \rho^{(0)}(z, \omega_{0,n}) + \sum_{p=1}^P N_p^{-1} \sum_{n=1}^{N_p} (\rho^{(p)}(z, \omega_{p,n}) - \rho^{(p-1)}(z, \omega_{p,n})).$$

The same concept can be applied to the computation of the correlation. Let c_0, v_0 denote the cost and the variance of $\rho^{(0)}$, respectively. For $p > 0$, c_p, v_p are the cost and variance of $\rho^{(p)} - \rho^{(p-1)}$, accordingly. Then, the overall cost and variance of multilevel Monte Carlo estimate are

$$C(P) := \sum_{p=0}^P N_p c_p$$

and

$$V(P) := \sum_{p=0}^P N_p^{-1} v_p,$$

respectively, see [22]. Finding the minimum value of the overall cost subject to the constraint that the overall variance is $V(P) = \epsilon^2$ at most is equivalent to finding the values of $\{N_p\}$ and Lagrange multipliers λ that simultaneously satisfy the equations defined by

$$(13) \quad \begin{cases} \nabla_{N_p} C(P) = \lambda \nabla_{N_p} (V(P) - \epsilon^2) & \text{for } p = 0, \dots, P, \\ V(P) = \epsilon^2. \end{cases}$$

By solving the linear system of equations (13), we obtain that when

$$(14) \quad N_p \sim \sqrt{\frac{\lambda v_p}{c_p}}, \quad \text{where} \quad \lambda = \left(\frac{\sum_{p=0}^P \sqrt{c_p v_p}}{\epsilon^2} \right)^2,$$

the minimum overall cost is achieved, see [22]. The computation at the low levels is cheaper compared to calculations at the high levels, i.e., c_p is a monotonically increasing function of the polynomial degree p , and the variance v_p is a monotonically decreasing function of degree p . Equation (14) suggests that the optimal number of samples decreases like $\sqrt{v_p/c_p}$ with increasing degrees. Specifically, when increasing from $p-1$ to p , the number of samples should decrease by a factor of

$$\gamma_p := \sqrt{\frac{v_{p-1}}{v_p}} \sqrt{\frac{c_p}{c_{p-1}}}.$$

6. NUMERICAL EXPERIMENTS

All experiments in this article are performed on the Eiger cluster of the Swiss National Supercomputing Centre. Each node is equipped with 2 x AMD 7742 CPU@2.2 GHz processors. The calculations are performed using up to 64 MPI processes, each consisting of up to 20 OpenMP threads, for a total of up to 1280 cores. The implementation of the barycentric interpolation has been integrated into **Bembe1** (the BEM-based engineering library, www.bembe1.eu), see [17]. The latter is also used for the assembly of the boundary integral formulation.

6.1. General setup. In the numerical experiments, we consider a torus (bounding box: $[-1, 1] \times [-1, 1] \times [-1, 1]$) and Michelangelo's David (bounding box: $[-1, 1] \times [-1, 1] \times [-0.2, 0.2]$) for the reference scatterer D_0 , respectively. Both of domains have a diameter of 2. The artificial interface T (24 patches) is given by the cuboid $[-2, 2] \times [-2, 2] \times [-2, 2]$ in both cases, see Figure 4. The artificial interface undergoes discretization using tensor-product polynomials of degree 8 on each patch. Subsequently, Cauchy data for the artificial interface is derived by conducting 1944 point evaluations on T . For the Helmholtz equation, we consider the incident plane wave with wavenumber $\kappa = 5$ and direction $\mathbf{d} = (1, 0, 0)$. Regarding the random deformation field, we consider the deformation field given by $\mathbb{E}[\boldsymbol{\chi}](\hat{\mathbf{x}}) = \hat{\mathbf{x}}$ and

$$\text{Cov}[\boldsymbol{\chi}](\hat{\mathbf{x}}, \hat{\mathbf{x}}') = \begin{bmatrix} k_{\frac{3}{2}}(20r) & 10^{-4}k_{\infty}(4r) & 10^{-4}k_{\infty}(4r) \\ 10^{-4}k_{\infty}(4r) & k_{\frac{3}{2}}(20r) & 10^{-4}k_{\infty}(4r) \\ 10^{-4}k_{\infty}(4r) & 10^{-4}k_{\infty}(4r) & k_{\frac{3}{2}}(20r) \end{bmatrix}.$$

The random field is computed by the pivoted Cholesky decomposition with an accuracy of 10^{-3} . This leads to the parameter dimension $m = 2218, 5563$ for the torus and David, respectively. Herein, we set the polynomial degree of the barycentric interpolation to 20 for the torus and to 10 for David. This results in 6516 landmark points for the torus consisting of 16 patches and 18702 landmark points for David consisting of 187 patches. In the deformation model, we set the magnitude of the random perturbation $\alpha = 0.07$, such that all realisations of random scatterers are inside the artificial interface T . This

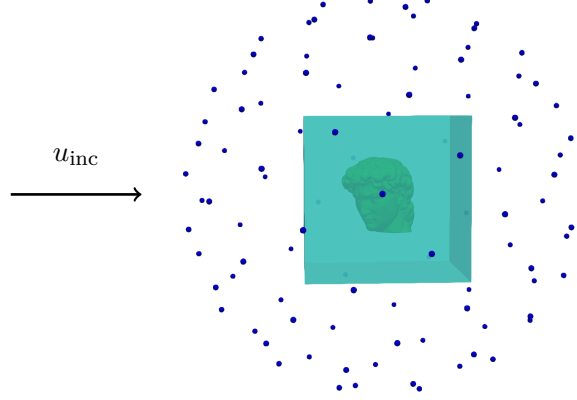


FIGURE 4. Setup for the numerical experiments on the David geometry. One hundred blue points are evaluation points. The artificial interface T is the cuboid $[-2, 2]^3$. The innermost object inside T is the scatterer. The incident plane wave is considered with wavenumber $\kappa = 5$ and direction $\mathbf{d} = [1, 0, 0]^\top$.

	$p = 0$	$p = 1$	$p = 2$	$p = 3$	$p = 4$	$p = 5$	$p = 6$
t	0.02637s	0.1139s	0.3403s	0.8488s	1.835s	3.742s	7.679s
$DOFs$	64	144	256	400	576	784	1024

TABLE 1. Number of degrees of freedom of the boundary element solver on the torus for different polynomial degrees p and fixed spatial refinement level $\ell = 1$.

results in a maximal possible relative displacement of 45% for the torus and 49% for David. Three different realisations each scatterer are visualised in Figure 8 and Figure 9 for the torus and David, respectively.

6.2. Boundary element method based on p -refinement. We start by numerically testing the exponential convergence rate of the maximum potential error evaluated at 100 points in free space with respect to the polynomial degree p . To this end, we consider the first realization of the random scatterers from Figure 5 and Figure 6. The evaluation points are uniformly distributed on a sphere with a radius 5. The number of the degrees of freedom (DOF) are shown in Table 1 for the torus and in Table 2 for David, where we use p -refinement at level $\ell = 1$. When increasing p by one, the degrees of freedom and the computation time in seconds are multiplied by a factor between 2 and 3, which is less than the numbers for h -refinement reported in [16]. The real parts of scattered waves by three realizations of each scatterer are depicted in Figure 8 and Figure 9 for the torus and David, respectively.

6.3. p -Multilevel Monte Carlo. From (2), the singular values of the chosen Matérn kernel with $\nu = \frac{3}{2}$ asymptotically decay like $\sigma_k \sim k^{-1.25}$. We numerically compute the first 2000 largest singular values of the covariance

	$p = 0$	$p = 1$	$p = 2$	$p = 3$	$p = 4$	$p = 5$
t	1.308s	1.351s	3.56s	11.87s	33.9s	101.8s
$DOFs$	748	1683	2992	4675	6732	9163

TABLE 2. Number of degrees of freedom of the boundary element solver on David for different polynomial degrees p and fixed spatial refinement level $\ell = 1$.

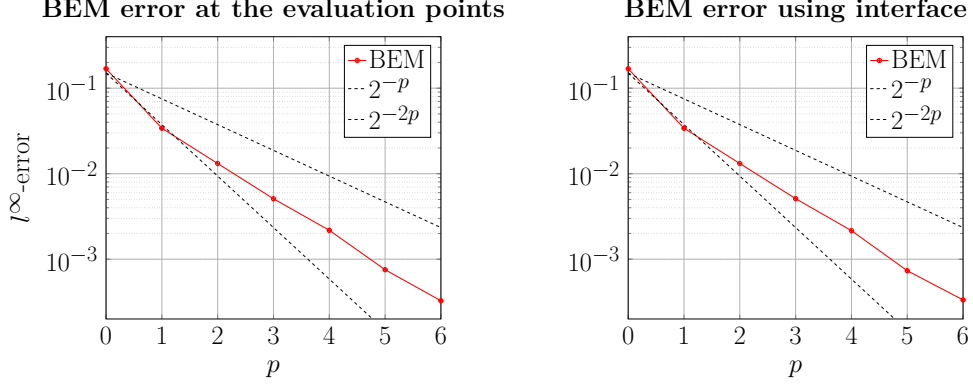


FIGURE 5. Convergence of boundary element solver on one realisation of the random torus.

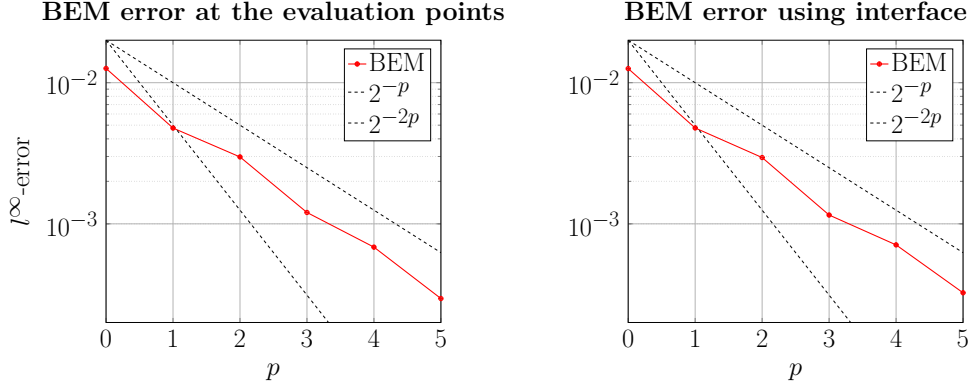


FIGURE 6. Convergence of boundary element solver on one realisation of the random David.

evaluated at the landmark points. The numerical result shows the decay rates are even slower than the theoretical asymptotical rate in the case of David, see Figure 7. This is caused by the multiplicity 3 of each eigenvalue.

We rely on p -MLMC to speed up the QoI computations. With increasing levels, we decrease the number of samples by a factor of

$$\hat{\gamma}_p = \sqrt{\frac{\hat{v}_{p-1}}{\hat{v}_p}} \sqrt{\frac{\hat{c}_p}{\hat{c}_{p-1}}}.$$

Herein, \hat{v}_p and \hat{c}_p are estimated variance and time complexity for each polynomial degree p , respectively. In the experiments, the approximations

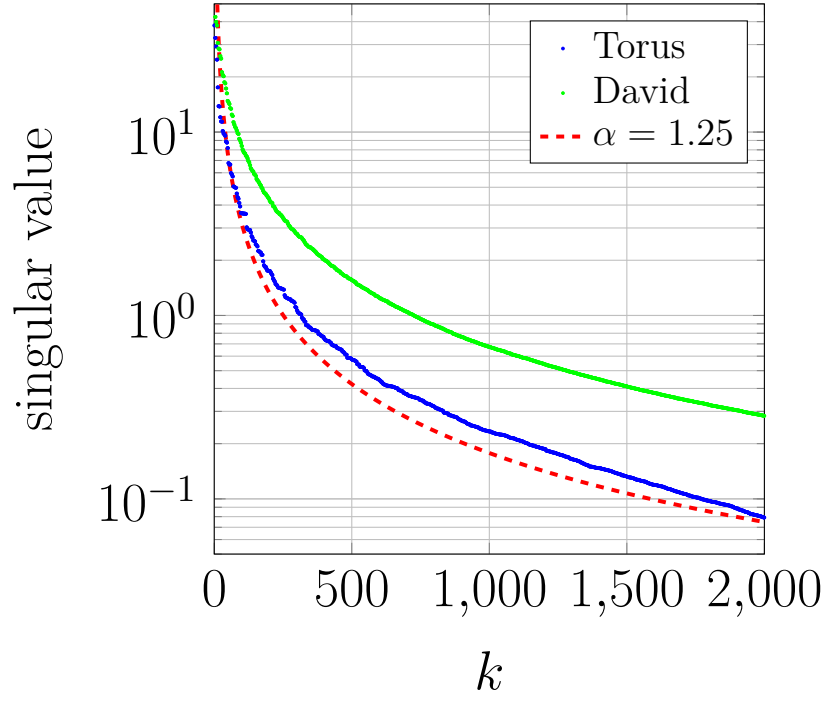


FIGURE 7. Numerical approximation of the singular values of the Karhunen-Loève expansion for the model under consideration.

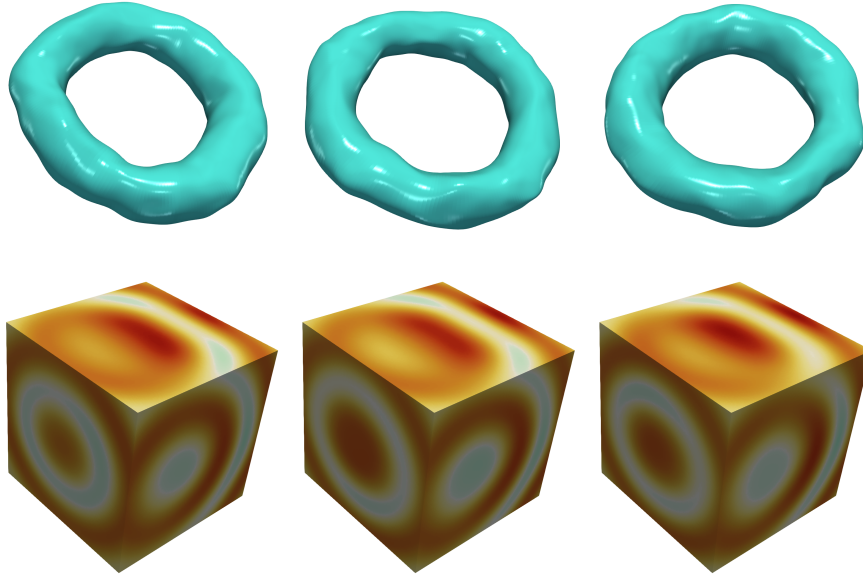


FIGURE 8. Realizations of the scatterer (torus) and the scattered wave at the interface.

are obtained using 64 samples. The number of samples at the highest polynomial degree P is fixed to 128. The number of samples increases from

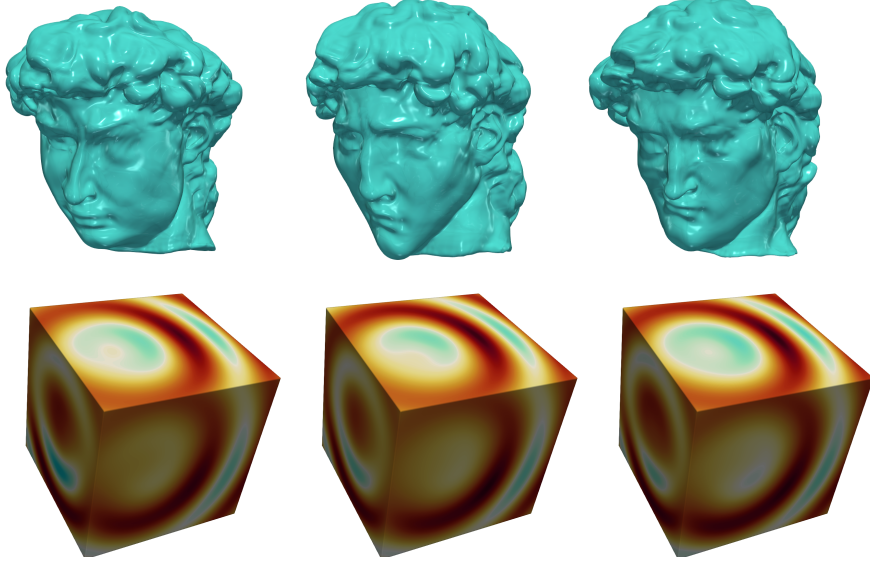


FIGURE 9. Realizations of the scatterer (David) and the scattered wave at the interface.

	$p = 0$	$p = 1$	$p = 2$	$p = 3$	$p = 4$	$p = 5$	$p = 6$
reference	98470	47260	5969	2137	1029	389	128
p -MLMC	32390	15540	1963	703	338	128	-

TABLE 3. Number of samples for the different polynomial degrees p for the p -MLMC on the torus. A p -MLMC solution with highest degree 6 is used as reference.

	$p = 0$	$p = 1$	$p = 2$	$p = 3$	$p = 4$	$p = 5$
reference	155500	10550	2821	1491	368	128
p -MLMC	54010	3666	980	518	128	-

TABLE 4. Number of samples for the different polynomial degrees p for the p -MLMC on David. A p -MLMC solution with degree 5 is used as reference.

p to $p - 1$ according to the factor $\hat{\gamma}_p$. This leads to the number of samples at each polynomial degree level p shown in Table 3 and Table 4 for the torus and David, respectively. To benchmark the convergence, we use the p -multilevel Monte Carlo solution with the highest polynomial degree $P + 1$ as reference. In this study, we set P to 5 and 4 for the torus and David, respectively. Notably, the higher number of paths in David's case compensates for its lower polynomial degree, in contrast to the torus.

From Figure 10 (for the torus) and Figure 11 (for David), the maximum error of the expectation and correlation at 100 evaluation points is reduced by a factor approximately between 2 and 4 when increasing p by 1 (applicable for most values of p) in both cases. We report both, the error for the direct evaluation and the evaluation using the artificial interface. Both errors are

comparable. The top row of each figure corresponds to the expectation and the bottom row to the correlation. In all cases, the overall convergence rate is almost the same as for the boundary element solver alone. And the maximum error of the expectation at the highest level P approaches a similar scale (around 10^{-3}) as the error for the boundary element solver alone.

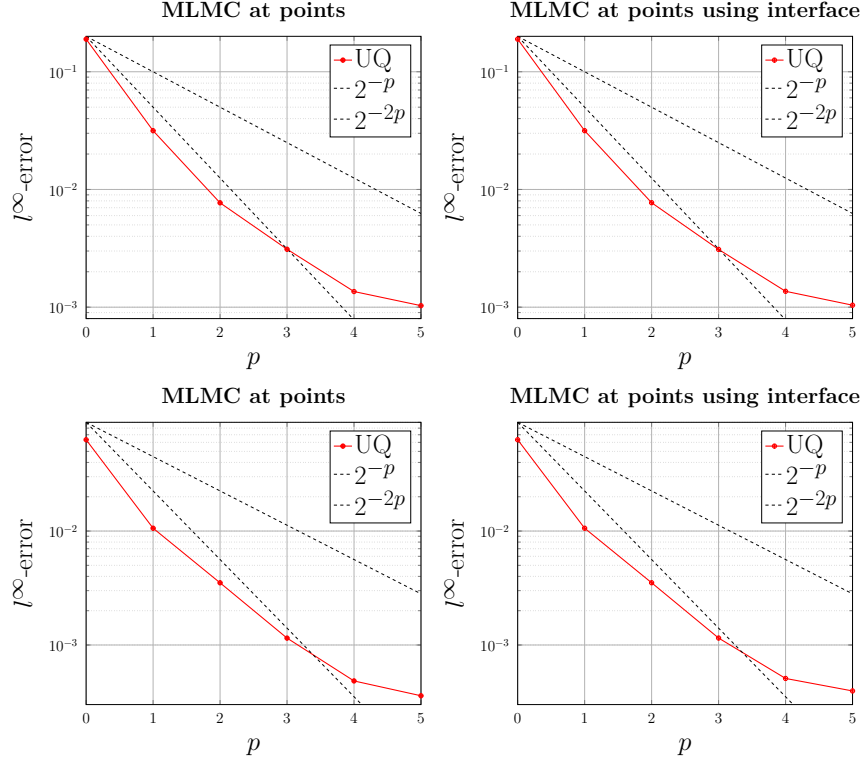


FIGURE 10. Convergence of the expectation (top) and correlation (bottom) towards the reference solution for the torus.

7. CONCLUSION

In this article, we considered the time-harmonic acoustic scattering problem from objects subject to large and rough random deviations. In this setting, neither QMC nor sparse grid approaches for quadrature based computation of statistical moments are applicable. Perturbation approaches are not suitable due to their restriction to rather small deviations. To overcome the prohibitive computational cost the combination of Monte Carlo sampling and highly refined meshes, we have considered a p -multilevel Monte Carlo approach. To this end, we have described how we may generate conforming multi-patch NURBS surfaces based on complex geometries given by triangular meshes. We have provided an algorithm by means of barycentric interpolation that allows to efficiently model even rough deformation fields with low Sobolev regularity of the covariance function and a slowly decaying Karhunen-Loève expansion. Thanks to the suggested boundary integral approach, we do not require nested meshes to evaluate the approximations for different polynomial

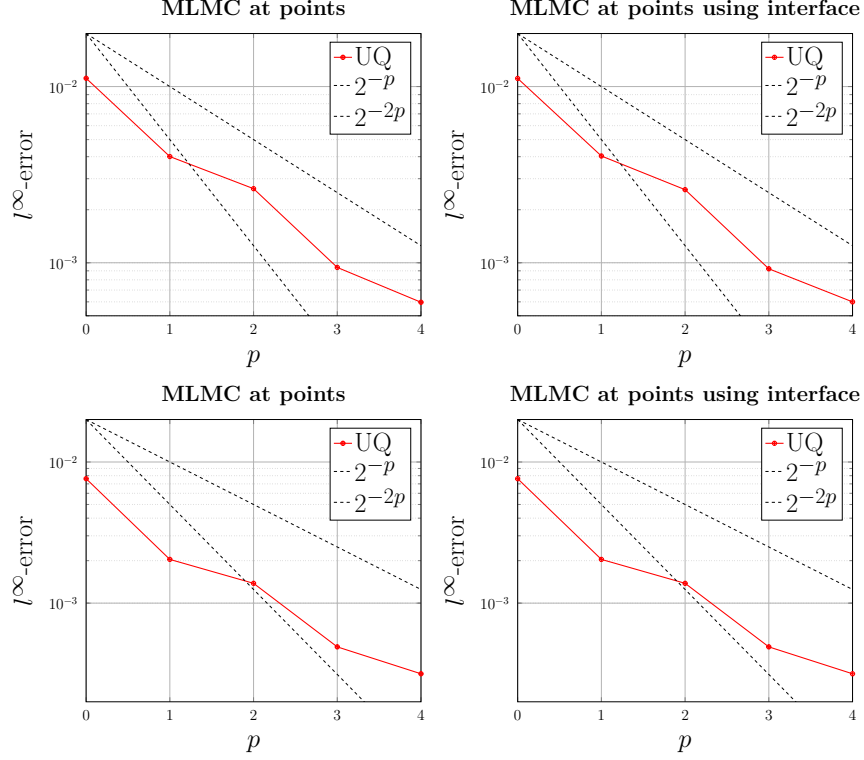


FIGURE 11. Convergence of the expectation (top) and correlation (bottom) towards the reference solution for David.

degrees. Our numerical studies on complex geometries clearly demonstrate the advantages of this approach, in particular the ability of handling large and rough random perturbations and the capability of approximating the scattered wave in free space.

REFERENCES

- [1] R. Aylwin, C. Jerez-Hanckes, C. Schwab, and J. Zech. Domain uncertainty quantification in computational electromagnetics. *SIAM/ASA Journal on Uncertainty Quantification*, 8(1):301–341, 2020.
- [2] J.-P. Berrut and L. N. Trefethen. Barycentric lagrange interpolation. *SIAM review*, 46(3):501–517, 2004.
- [3] T. Bin Masood, J. Budin, M. Falk, G. Favelier, C. Garth, C. Gueunet, P. Guillou, L. Hofmann, P. Hristov, A. Kamakshidasan, C. Kappe, P. Klacansky, P. Laurin, J. Levine, J. Lukasczyk, D. Sakurai, M. Soler, P. Steneteg, J. Tierny, W. Usher, J. Vidal, and M. Wozniak. An overview of the Topology ToolKit. In *IEEE Workshop on Topological Data Analysis and Visualization*, 2019.
- [4] P. Blondeel, P. Robbe, C. Van hoorickx, S. François, G. Lombaert, and S. Vande-walle. p-refined multilevel quasi-monte carlo for galerkin finite element methods with applications in civil engineering. *Algorithms*, 13(5):110, 2020.
- [5] F. Bonizzoni and F. Nobile. Perturbation analysis for the darcy problem with log-normal permeability. *SIAM/ASA Journal on Uncertainty Quantification*, 2(1):223–244, Jan. 2014.
- [6] H.-J. Bungartz and M. Griebel. Sparse grids. *Acta Numerica*, 13:147–269, May 2004.

- [7] R. Caflisch. Monte Carlo and quasi-Monte Carlo methods. *Acta Numerica*, 7:1–49, 1998.
- [8] R. E. Caflisch. Monte Carlo and quasi-Monte Carlo methods. *Acta Numerica*, 7:1–49, Jan. 1998.
- [9] M. Campen. Partitioning surfaces into quad patches. In *Eurographics (Tutorials)*, 2017.
- [10] J. E. Castrillón-Candás, F. Nobile, and R. F. Tempone. Analytic regularity and collocation approximation for elliptic PDEs with random domain deformations. *Computers & Mathematics with Applications*, 71(6):1173–1197, 2016.
- [11] J. E. Castrillón-Candás, F. Nobile, and R. F. Tempone. A hybrid collocation-perturbation approach for PDEs with random domains. *Advances in Computational Mathematics*, 47(3):40, June 2021.
- [12] D. Colton and R. Kress. *Inverse Acoustic and Electromagnetic Scattering*. Springer, Berlin-Heidelberg-New York, 2nd edition, 1997.
- [13] M. Darmon, V. Dorval, and F. Baqué. Acoustic scattering models from rough surfaces: A brief review and recent advances. *Applied Sciences*, 10(22):8305, 2020.
- [14] J. Dölz. A higher order perturbation approach for electromagnetic scattering problems on random domains. *SIAM/ASA Journal on Uncertainty Quantification*, 8(2):748–774, Jan. 2020.
- [15] J. Dölz and H. Harbrecht. Hierarchical matrix approximation for the uncertainty quantification of potentials on random domains. *Journal of Computational Physics*, 371:506–527, Oct. 2018.
- [16] J. Dölz, H. Harbrecht, C. Jerez-Hanckes, and M. Multerer. Isogeometric multilevel quadrature for forward and inverse random acoustic scattering. *Computer Methods in Applied Mechanics and Engineering*, 388:114242, 2022.
- [17] J. Dölz, H. Harbrecht, S. Kurz, M. Multerer, S. Schöps, and F. Wolf. Bembel: The fast isogeometric boundary element C++ library for Laplace, Helmholtz, and electric wave equation. *SoftwareX*, 11:100476, 2020.
- [18] J. Dölz, H. Harbrecht, and M. Multerer. Solving acoustic scattering problems by the isogeometric boundary element method. 2023.
- [19] J. Dölz and F. Henríquez. Parametric shape holomorphy of boundary integral operators with applications, May 2023.
- [20] S. Dong, P.-T. Bremer, M. Garland, V. Pascucci, and J. C. Hart. Spectral surface quadrangulation. In *ACM SIGGRAPH 2006 Papers*, pages 1057–1066. 2006.
- [21] M. B. Giles. Multilevel Monte Carlo path simulation. *Operations Research*, 56(3):607–617, 2008.
- [22] M. B. Giles. Multilevel Monte Carlo methods. *Acta Numerica*, 24:259–328, 2015.
- [23] I. G. Graham, F. Y. Kuo, J. A. Nichols, R. Scheichl, C. Schwab, and I. H. Sloan. Quasi-Monte Carlo finite element methods for elliptic pdes with lognormal random coefficients. *Numerische Mathematik*, 131:329–368, 2015.
- [24] A.-L. Haji-Ali, H. Harbrecht, M. D. Peters, and M. Siebenmorgen. Novel results for the anisotropic sparse grid quadrature. *Journal of Complexity*, 47:62–85, 2018.
- [25] H. Harbrecht, M. Peters, and R. Schneider. On the low-rank approximation by the pivoted Cholesky decomposition. *Applied Numerical Mathematics*, 62(4):428–440, 2012.
- [26] H. Harbrecht, M. Peters, and M. Siebenmorgen. On multilevel quadrature for elliptic stochastic partial differential equations. In J. Garcke and M. Griebel, editors, *Sparse Grids and Applications*, volume 88 of *Lecture Notes in Computational Science and Engineering*, pages 161–179, Berlin-Heidelberg, 2012. Springer.
- [27] H. Harbrecht, M. Peters, and M. Siebenmorgen. Analysis of the domain mapping method for elliptic diffusion problems on random domains. *Numerische Mathematik*, 134(4):823–856, 2016.
- [28] H. Harbrecht, R. Schneider, and C. Schwab. Sparse second moment analysis for elliptic problems in stochastic domains. *Numerische Mathematik*, 109(3):385–414, 2008.
- [29] S. Heinrich. Multilevel Monte Carlo methods. In *Lecture Notes in Large Scale Scientific Computing*, pages 58–67, London, 2001. Springer.

- [30] R. Hiptmair, L. Scarabosio, C. Schillings, and Ch. Schwab. Large deformation shape uncertainty quantification in acoustic scattering. *Advances in Computational Mathematics*, 44(5):1475–1518, Oct. 2018.
- [31] W. Huang and M. Multerer. Isogeometric analysis of diffusion problems on random surfaces. *Applied Numerical Mathematics*, 179:50–65, 2022.
- [32] C. Jerez-Hanckes, C. Schwab, and J. Zech. Electromagnetic wave scattering by random surfaces: Shape holomorphy. *Mathematical Models and Methods in Applied Sciences*, 27(12):2229–2259, 2017.
- [33] B. Kachoyan and C. Macaskill. Acoustic scattering from an arbitrarily rough surface. *The Journal of the Acoustical Society of America*, 82(5):1720–1726, 1987.
- [34] C. Macaskill and B. Kachoyan. Numerical evaluation of the statistics of acoustic scattering from a rough surface. *The Journal of the Acoustical Society of America*, 84(5):1826–1835, 1988.
- [35] M. D. Multerer. A note on the domain mapping method with rough diffusion coefficients. *Applied Numerical Mathematics*, 145:283–296, 2019.
- [36] H. E. Salzer. Lagrangian interpolation at the chebyshev points x_n , $\nu \equiv \cos(\nu\pi/n)$, $\nu = 0(1)n$; some unnoted advantages. *The Computer Journal*, 15(2):156–159, 1972.
- [37] J. Tierny, G. Favelier, J. A. Levine, C. Gueunet, and M. Michaux. The Topology ToolKit. *IEEE Transactions on Visualization and Computer Graphics (Proc. of IEEE VIS)*, 2017. <https://topology-tool-kit.github.io/>.
- [38] V. Twersky. Reflection and scattering of sound by correlated rough surfaces. *The Journal of the Acoustical Society of America*, 73(1):85–94, 1983.
- [39] X. Wang. A constructive approach to strong tractability using quasi-Monte Carlo algorithms. *J. Complexity*, 18:683–701, 2002.
- [40] D. Xiu and D. M. Tartakovsky. Numerical methods for differential equations in random domains. *SIAM Journal on Scientific Computing*, 28(3):1167–1185, 2006.

Email address: doelz@ins.uni-bonn.de

Email address: wei.huang@usi.ch

Email address: michael.multerer@usi.ch